

FEATURE ARTICLE

Real-Space Surface Crystallography from Ion Scattering

V. Bykov,[†] L. Houssiau,[‡] and J. W. Rabalais^{*,†}

Department of Chemistry, University of Houston, Houston, Texas 77204-5641, and Department des Sciences des Matériaux et des Procédés, Université Catholique de Louvain, PCPM-UCL, Place Croix du sud, 1B-1348 Louvain-la-Neuve, Belgium

Received: January 13, 2000; In Final Form: March 21, 2000

Ion beams in the kiloelectronvolt energy range impinging on crystal surfaces are atomic-size probes of the nanoscale magnifying and focusing “lenses” formed by the periodic structures. These lenses disperse the scattered and recoiled atom trajectories into macroscopic projections according to their velocities as a function of projectile/target atom masses and deflection angles. The resulting patterns reflect the near-surface interatomic vectors. The spatially and temporally resolved images of these patterns can now be acquired by means of new developments in ion scattering spectrometry, providing direct, element-specific, real-space projections of surface structure. The resulting scattering and recoiling imaging spectrometry (SARIS) provides unique capabilities for analyzing surface composition and structure and for investigating the interactions of ions with surfaces. A classical ion trajectory program called scattering and recoiling imaging code (SARIC) that simulates the spatial and time intensity distributions of the SARIS images has been developed. A quantitative comparison of experimental and simulated images is achieved by means of a two-dimensional reliability (*R*) factor. Examples of applications include experimental stereographic projections of the Ni(110) and Pt(111) surfaces, the termination layer of the CdS(0001) surface, the chemisorption of Cl₂ on Ni(110) and H₂ on Pt(111), and the atomic lenses in the Pt(111) surface.

1. Introduction

Adsorbates on surfaces occupy specific chemically active sites, and atoms of the surface itself often arrange themselves so as to have a different symmetry or different interlayer spacings from that of the bulk;¹ the former is known as “reconstruction” and the latter as “relaxation”. Knowledge of surface atomic positions is important for several applications, e.g., understanding reactive sites in catalysis, defining atomic templates for epitaxial film growth, and fabricating well-defined interfaces between different materials. From a heuristic viewpoint, we are interested in knowing if atomic sites and bond lengths in surfaces are as well-defined as those of the bulk and if there are important new phenomena to be derived therein. Although the many significant advances in surface science over the past three decades² have greatly increased our understanding of surface phenomena, the incessantly decreasing size of microelectronic devices and their requisite atomic-scale surface analysis drive the development of surface science techniques. Recent advances in ion scattering are reported herein through which the spatially and temporally resolved patterns of scattered and recoiled kiloelectronvolt (keV) ions and atoms from surfaces can be measured. Ion beams are probes of nanoscale magnifying and focusing “lenses” formed by periodic surface structures. These lenses disperse ion trajectories into macroscopic projections, the patterns of which reflect the near-surface interatomic

vectors in the form of blocking cones. The patterns form element-specific, real-space images of the crystallographic features, as shown in the cover figure. This figure presents a three-dimensional distribution of the scattered ion intensity for 4 keV He⁺ scattering from a Ni(110) surface. Atomic-scale resolution of surface structure can be obtained from such distributions.

The origin of scattering experiments has its roots in the development of modern atomic theory in the early 20th century. As a result of both the Rutherford experiment on the scattering of alpha particles by thin metallic foils and the Bohr theory of atomic structure, a consistent model of the atom as a small massive nucleus surrounded by a large swarm of light electrons was confirmed. It was then realized that the inverse process, namely, analysis of the scattering patterns of ions from crystals, could provide information on composition and structure. This analysis is straightforward because the kinematics of keV atomic collisions is accurately described by classical mechanics. Such scattering occurs as a result of the mutual Coulomb repulsion between the colliding atomic cores, i.e., the nucleus plus core electrons. The scattered primary atom loses some of its energy to the target atom which, in turn, recoils into a forward direction, as shown in Figure 1a. The final energies of the scattered and recoiled atoms and the directions of their trajectories are determined by the masses of the pair of atoms involved and the closeness of the collision.

Low-energy (1–30 keV) ion scattering spectrometry (ISS) had its beginning as a modern surface analysis technique with the 1967 work of Smith.³ Over the next thirty years, it was

* Author to whom correspondence should be addressed.

[†] University of Houston.

[‡] Université Catholique de Louvain.

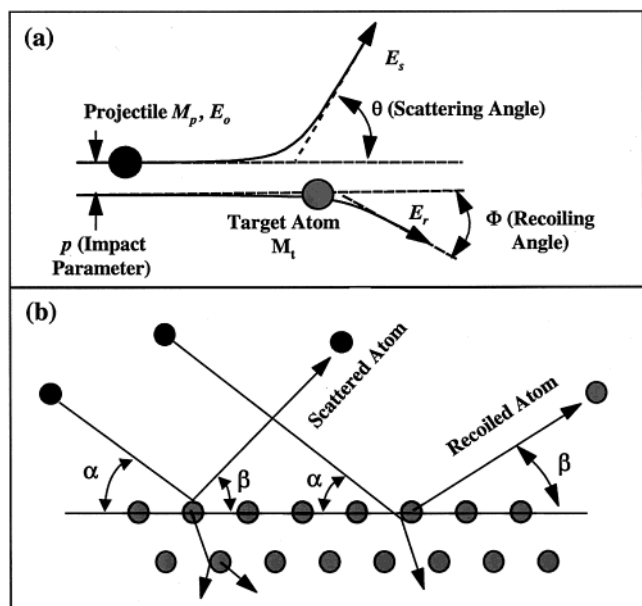


Figure 1. (a) Two-body collision for a projectile of mass M_p and kinetic energy E_o approaching a stationary target atom of mass M_t with an impact parameter p . (b) Quasi-single scattering (SS) and direct recoiling (DR) from a surface with incident angle α , exit angle β , and scattering angle θ .

clearly demonstrated^{4–18} that direct surface compositional and structural information could be obtained from ISS. The introduction of time-of-flight (TOF) methods¹⁹ for detection of both neutrals and ions greatly improved the sensitivity of ISS, leading to the development of time-of-flight scattering and recoiling spectrometry (TOF-SARS).^{20,21} A large, time-gated, position-sensitive microchannel plate detector was introduced in 1998 to obtain scattering and recoiling images, leading to the development of scattering and recoiling imaging spectrometry (SARIS).²² This article describes the recently developed SARIS technique and the type of new information that it can provide. It contains both new and some previously published examples.

2. Kinematics of Ion–Surface Collisions

2.1. Energy and Intensity Distributions. The dynamics of ion–surface scattering at energies exceeding several hundred electronvolts can be described by a binary collision approximation (BCA)^{23–25} that treats the projectile–target interaction as a series of sequential two-body collisions. The simplest case of ion–surface scattering phenomena is quasi-single scattering (SS), which represents the case of one large angle deflection that may be preceded and/or followed by a few small angle deflections, as shown in Figure 1b. This typically produces a sharp scattering peak whose energy is near that of the BCA single-collision energy. The energies of scattered and recoiled particles in single-scattering (SS) collisions can be derived from the laws of conservation of energy and momentum. The energy E_s of a projectile of mass M_p scattered from a stationary target of mass M_t is given as

$$E_s = \frac{E_o}{(1 + A)^2} [\cos \theta \pm (A^2 - \sin^2 \theta)^{1/2}]^2 \quad (1)$$

where $A = M_t/M_p$ and E_o is the initial energy of the projectile. If the mass of the impinging particle is less than or equal to that of the target atom, then $A \geq 1$, and only the positive sign

applies. If the mass of the ion is greater than that of the target atom, both signs in eq 1 apply. The energy of the scattered particle is then found to be a double-valued function of the scattering angle θ , i.e., there are two distinct E_s values for each possible value of θ . For the case of $A < 1$, the maximum SS scattering angle is

$$\theta_{\max} = \sin^{-1} A \quad (2)$$

For angles greater than θ_{\max} , only multiple scattering can occur. Direct recoil (DR)²⁶ of surface atoms produces energetic atoms that have a narrow velocity distribution. DR particles are those atoms that are recoiled from the surface layers as a result of a direct collision of the primary ion, as shown in Figure 1b. They escape from the surface with little energy loss through collisions with neighboring atoms. The energy E_r of a DR surface atom can be expressed as

$$E_r = E_o \frac{4A}{(1 + A)^2} \cos^2 \phi \quad (3)$$

From kinematic considerations, DR is observed only in the forward-scattering direction for which $\phi < 90^\circ$.

The intensity of single scattering I_i from an element i in the solid angle $\Delta\Omega$ is proportional to the initial beam intensity I_o , the concentration of the scattering centers N_i , the differential scattering cross section $d\sigma(\theta)/d\Omega$, and the shadowing $f_{si}(\alpha, \delta_{in})$ and blocking $f_{bi}(\beta, \delta_{out})$ coefficients for the i th component on the surface, where α , β , and δ are the incident, exit, and azimuthal angles, respectively. The resulting expression is

$$I_i \approx I_o N_i f_{si} f_{bi} \frac{d\sigma}{d\Omega} \Delta\Omega \quad (4)$$

The neutralization probability does not enter into eq 4 because both ions and neutrals are detected simultaneously by TOF. An expression similar to eq 4 is applicable for recoiling intensity evaluation. All elements, including hydrogen, can be analyzed by either scattering, recoiling, or both techniques. TOF peak identification of SS and DR is straightforward using eqs 1 and 3.

2.2. Shadowing and Blocking. When a beam of parallel energetic ions interacts with a target atom, the target-atom core of size ~ 0.01 nm acts as a virtual point source, scattering the atoms with a near isotropic intensity distribution. This phenomenon is due to the short de Broglie wavelengths (~ 0.1 pm) of keV atoms, which constrain them to classical behavior, and their large collision cross sections ($\sim 1 \times 10^{-3}$ nm²), which provide sensitivity to only the near-surface region. Such atomic collisions are described qualitatively as “three-dimensional pool”²⁷ or quantitatively by classical mechanics.²⁸ Scattering of ions by a target atom produces an excluded region called a shadow cone behind the target atom into which no ion can penetrate, as shown in Figure 2a. There is zero flux density inside the cone, unit density far outside of the cone, and highly focused flux density at the boundary of the cone, as shown in Figure 2b. This anisotropic distribution of ion flux after interaction with a target atom is the basis of ISS structural determinations. If a neighboring atom lies in the focusing region, enhanced scattering and/or recoiling intensity is observed. TOF-SARS measures the intensity change due to the shadowing effect on neighboring atoms as a function of incident or azimuthal angle beam direction. A shadow cone originates from the interaction of an atom with collimated atoms from a flux of parallel ions (ion source in an ion beam line), resulting in a paraboloid cone shape

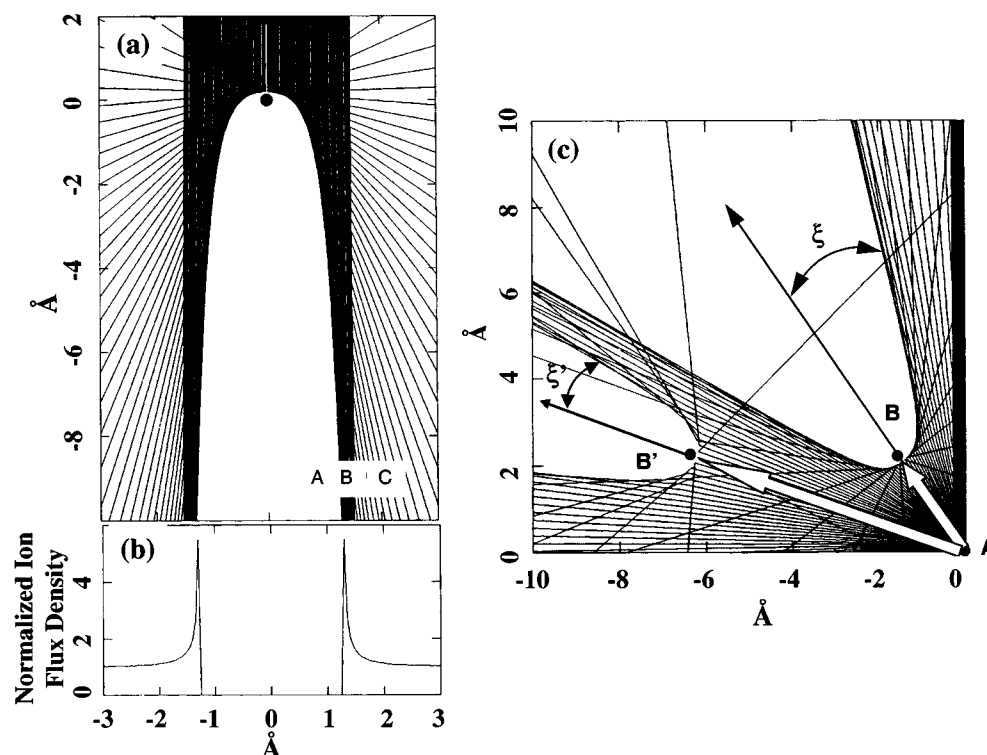


Figure 2. (a) Shadow cone of a Pt atom in a 4 keV Ne^+ beam, appearing with the overlapping of ion trajectories as a function of impact parameter. (b) Normalized ion flux distribution density across the shadow cone in part a. The flux density changes from 0 inside the shadow cone (A), to $\gg 1$ in the focusing region (B), converging to 1 away from the shadow cone edge (C). (c) Blocking cones of Pt atoms (B, B') cast by 4 keV Ne^+ scattered from another Pt atom (A), which acts as a "virtual emitter" of scattered atoms. The interatomic vectors and blocking angles ξ are shown. Note that $\xi \sim f(1/d)$, where d is the interatomic distance.

(Figure 2a). If a scattered-atom trajectory intersects the site position of a neighboring atom, the trajectory is deflected by the repulsive potential of the blocking atom. This results in a "blocking cone"²⁰ centered around the blocking atom. It can be regarded as an interaction of a target atom (blocking atom) with diverging ions emitted from a nearby point source (scattering atom). Unlike a shadow cone, a blocking cone diverges, as shown in Figure 2c. Scattered or recoiled atoms do not penetrate into these blocking cones but, instead, are focused along the edges of the cones, as shown in the cover figure. When viewed by a position-sensitive detector at a large distance from the surface, the features in the images are of macroscopic size because of the diverging nature of the hyperboloid-like cone shapes²⁶ and resulting trajectories. This magnification can be compared to an overhead projector: the virtual atomic source is the lamp, the blocking atoms are features in the transparency, and the detector is the screen. For ion scattering, the interatomic spacings d and the "blocking atom radius" r are of atomic size, while the source-to-image distance D is of macroscopic size, resulting in an image size R that is magnified by $D/d = R/r \sim 10^9$.

There is a large number of scatterer and blocker combinations in a solid. For ordered crystals, the periodicity and short interaction range (< 1 nm) of the atoms reduces this number of combinations to a tractable level. These scatterer and blocker combinations can be viewed as interatomic vectors (Figure 2) with a density of $\sim 10^{19} \text{ m}^{-2}$, resulting in reinforced focusing and blocking patterns. The projections of the interatomic vectors appear as regions of low intensity in the SARIS images because of the blocking of isotropically scattered ion trajectories from near-surface atoms. The resulting patterns allow direct construction of a model of the surface structure, providing the basis of SARIS.

3. Experiments and Simulations

3.1. Time-of-Flight Scattering and Recoiling Spectrometry (TOF-SARS). Analysis of a time-of-flight spectrum using the standard TOF-SARS technique provides the basis for understanding the SARIS images that follow. In TOF-SARS,²¹ a low keV, monoenergetic, mass-selected, pulsed noble gas ion beam is focused onto a sample surface, as shown in Figure 3. The velocity distributions of scattered and recoiled particles are measured by standard TOF methods, as described elsewhere.²⁹ A channel electron multiplier that has a small acceptance solid angle is used to detect ions and fast (> 800 eV) neutral species. The sample is rotated to measure ion scattering and recoiling anisotropy as a function of the incident (α) and azimuthal angles (δ) of the incident beam. Elemental analyses are achieved by converting the velocity distributions into energy distributions and relating those to the masses of the target atoms through kinematic relationships (eqs 1–3). Structural analyses are achieved by monitoring the scattered and recoiled particles as a function of both α and δ . The anisotropic features in these α - and δ -scans are interpreted by means of shadowing and blocking cone analyses.

3.2. Scattering and Recoiling Imaging Spectrometry (SARIS). A schematic drawing of the SARIS experimental setup is shown in Figure 4. The measurement couples time-of-flight techniques and a position-sensitive detector to capture both velocity- and spatially resolved patterns of scattered and recoiled atoms simultaneously. A pulsed ion beam²¹ of 3–25 keV rare gas ions, 5 ns pulse width, 30 kHz pulse rate, and $\sim 3 \times 10^3$ ions/pulse is used in the experiments. The velocities of the scattered and recoiled ions plus fast neutrals are analyzed by measuring their flight times from the sample to a position-sensitive microchannel plate (MCP) detector.²² The MCP is $75 \times 95 \text{ mm}^2$ and is equipped with a resistive anode encoder for

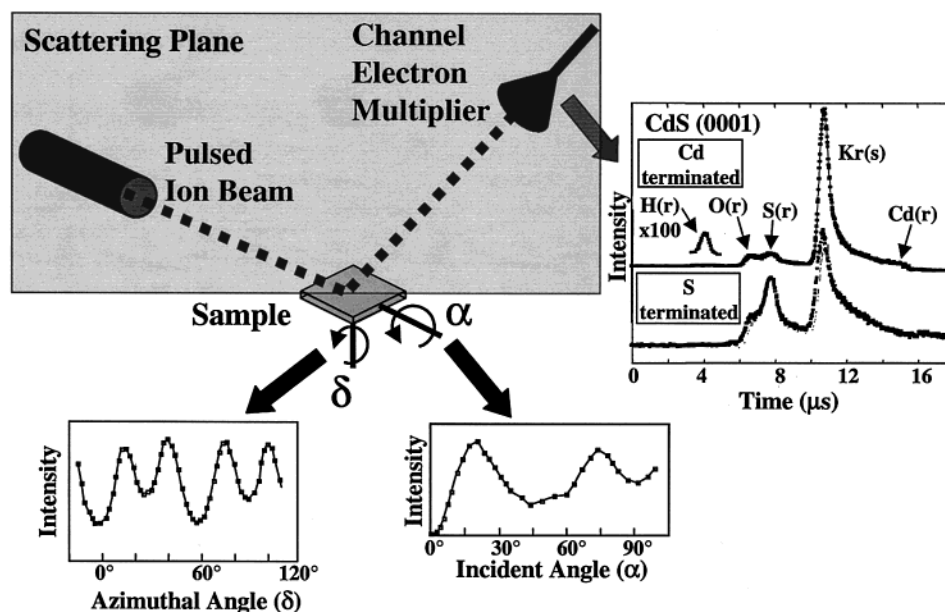


Figure 3. Schematic diagram of the TOF-SARS technique illustrating the plane of scattering formed by the ion beam, sample, and detector. Such spectra are collected with fixed positions of the ion beam, sample, and detector. To measure the incident angle α or azimuthal angle δ intensity variation of a peak in a TOF spectrum, the peak intensity is monitored as the sample is rotated about an axis that goes through its plane or through its normal, respectively. The TOF-SARS spectrum is for 4 keV Kr^+ ions on $\text{CdS}\{0001\}$. Kr(s) is krypton scattering from Cd; and Cd(r) , S(r) , O(r) , and H(r) are Cd, S, O, and H recoiling from Kr. The α and δ scans are for the Kr(s) intensity.

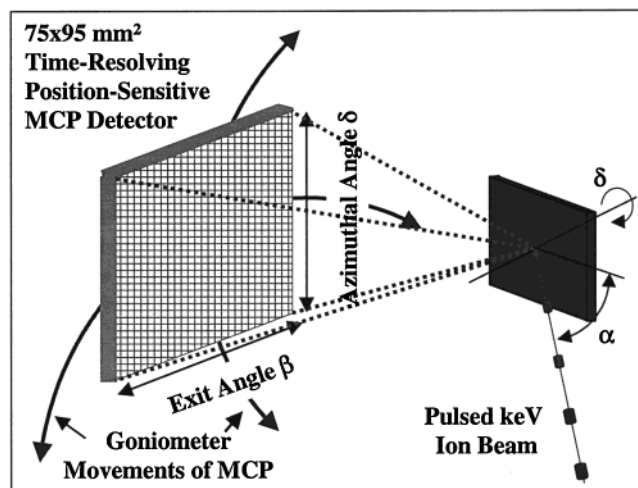


Figure 4. Schematic diagram of the SARIS experiment, showing the pulsed ion beam, sample, and MCP detector.

measuring the spatial distributions of arriving particles. It is gated so that it can be activated in time windows of several microsecond duration, which are appropriate for collection of specific scattered or recoiled species. Each window can be resolved into 256 time frames that can be as short as 10 ns each. The data are continuously stored in a buffer memory from which they can be transferred to a host computer. The preamplifier and control logic circuits have a dead time of ~ 300 ns, giving a maximum data acquisition rate of $\sim 3\text{M}$ cts/s. Good statistics are obtained by time averaging over ~ 1 s. Instrumental details are provided elsewhere.²²

3.3. Scattering and Recoiling Imaging Code (SARIC). SARIC^{30,31} is a classical ion trajectory simulation program that has been developed in our laboratory for simulation of the temporal and spatial distribution of the intensities from ion scattering spectra. The code is based on the BCA and allows simulations of interatomic interactions using several different standard potential functions to follow the three-dimensional

motions of atomic particles. Quasi-simultaneous interactions between several atoms are considered, thereby modeling the three-dimensional effects produced by the focusing atomic lenses of crystal structures. Vibrational motion is treated as an isotropic displacement of the crystal atoms, which is randomly chosen from a Gaussian distribution with a width corresponding to a root-mean-square displacement about the lattice sites. Our studies have shown that SARIC provides interpretations of the scattering and recoiling patterns in terms of the ion trajectories responsible for the specific features. A two-dimensional reliability (R) factor³² has been developed for the quantitative comparison of experimental and simulated images. Details of the code are described elsewhere.^{30,31}

4. Azimuthal Equidistant Mapping and Projection of SARIGrams

The angular dispersion of scattered and recoiled particles is directly related to the structure of the sample under investigation. The anisotropic features observed correspond to both in- and out-of-plane scattering and recoiling processes. By varying the relative orientation of the MCP with respect to the sample using a goniometer, it is possible to collect particles leaving the target in a range of almost 2π steradians (sr). Different scattering and recoiling phenomena^{33,34} can be assessed by collecting images at different MCP positions and time intervals. To handle the abundance of structural information^{35–39} resulting from such measurements, it is desirable to display the angular relationship between crystal lattice planes and features of the SARIS images in the form of an azimuthal equidistant mapping and projection into SARIGrams. Consider an *imaginary* hemispherical detector with the sample surface at the center of the hemisphere, as shown in Figure 5. All particles leaving the sample surface within 2π sr can be captured by such a detector. The MCP can be rotated to any position on the surface of such a hemisphere. Such a position-sensitive MCP is in the shape of a planar rectangle, resulting in distortion of the angular relations expected on a hemisphere. The coordinates (x_d , y_d) of each pixel on the

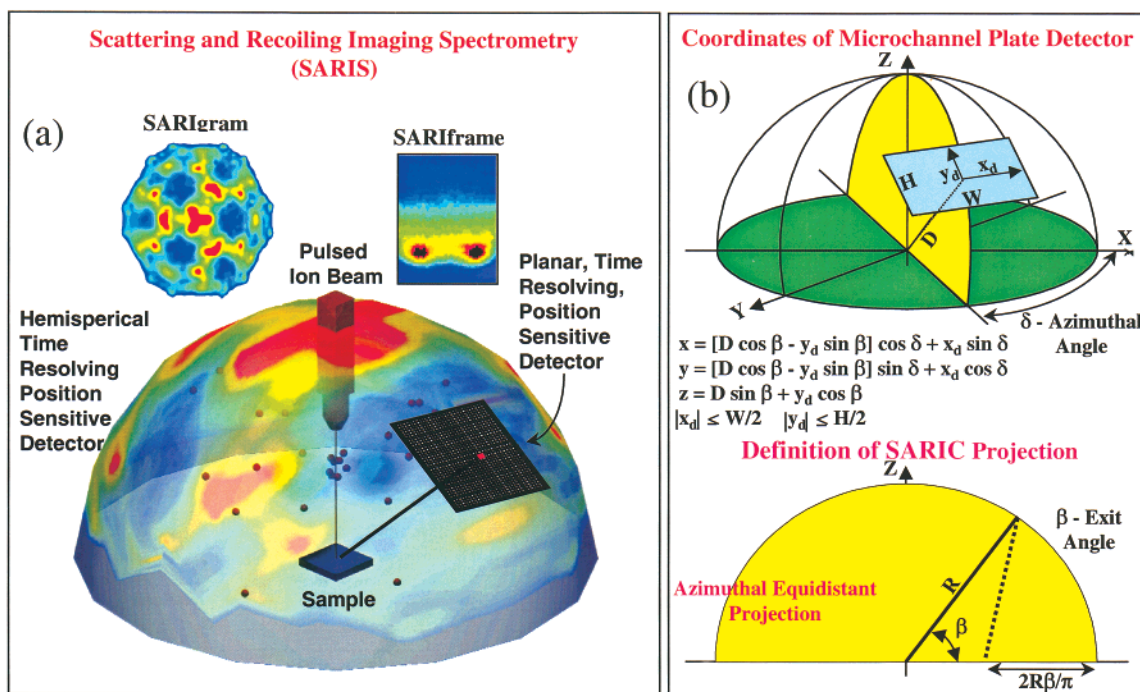


Figure 5. (a) Hypothetical hemispherical detector, simulated SARIGram, and experimental SARIFrame for 4 keV Ne^+ scattering from Pt(111). (b) Coordinates of the MCP detector and definition of the SARIC azimuthal equidistant projection.

MCP can be transformed to the corresponding angular coordinates on a hemisphere by using the direction cosines describing the spatial orientation of the vector that connects the center of the hemisphere to the detector pixel. Details are shown in Figure 5, where D is the target to detector distance, H and W are the detector height and width, and β and δ are the particle exit and azimuthal angles, respectively. When projecting the vector (x, y, z) onto the base plane (x, y) of the hemisphere, it is desirable to keep the same projected azimuth and to have the distance from the center to projection point be a linear measure of the vector exit angle β . Such a transformation provides a portion of an azimuthal equidistant projection,^{40,41} called a SARIGram, on which the angular relations between the crystallographic planes and poles can be related to the SARIS image, as shown in Figure 5. By rotating the MCP to different positions on the hemisphere, it is possible to obtain a complete projection. Having a 3D spatial intensity distribution mapped onto the 2D plot, it is possible to directly associate the features observed on the map with crystallographic directions characteristic for a given type of crystal bulk unit cell. The advantage of SARIGrams is as follows. The image areas of low intensity, so-called blocking cones, appear in the plot as slightly distorted circles, reflecting the fact that a normal cross section of such a cone is indeed a circle. The diameter of such a circle measured along the radial coordinate is directly related to the angular size of the blocking cone. In the mapping of individual SARIS images onto the hemispherical surface, the intensity measured by a pixel of the MCP is transformed to an equivalent solid angle increment on the hemispherical surface and then projected onto the SARIGram.

To determine the major crystallographic directions along which the characteristic features of the intensity distributions of the SARIGram are observed, consider the general case of a crystal bulk unit cell specified by three noncoplanar vectors \mathbf{v}_1 , \mathbf{v}_2 , and \mathbf{v}_3 defined by their lengths v_1 , v_2 , and v_3 and pairwise angles γ_{12} , γ_{23} , and γ_{13} . The spatial orientation of the unit cell is determined by the Miller indices of a facet of interest $(k, l,$

$m)$, where the $\mathbf{v} = [k, l, m]$ vector is parallel to the Z axis (surface normal), and the angle between \mathbf{v}_1 and the (x, z) plane, i.e., the surface azimuthal angle, is δ . Next, we find the components of all three unit cell vectors and then decompose any arbitrary direction vector ω into $\{\mathbf{v}_1, \mathbf{v}_2, \mathbf{v}_3\}$ space. From the definition of the bulk unit cell, the arbitrary direction vector can be written as

$$(\mathbf{v}_i \mathbf{v}_j) = v_i v_j \cos \gamma_{ij}; \quad i, j = 1, 2, 3 \quad (5)$$

The condition $\mathbf{v} \parallel Z$ is equivalent to $(\dot{\mathbf{v}} \epsilon_z) = |\mathbf{u}|$, where $\{\epsilon_x, \epsilon_y, \epsilon_z\}$ is an orthonormal basis of the Cartesian system of coordinates. With a knowledge of all nine components of \mathbf{v}_1 , \mathbf{v}_2 , and \mathbf{v}_3 , any vector ω given by the (x, y) coordinates of its SARI projection can be decomposed into its ω_1 , ω_2 , and ω_3 components. The integer parts of the ω_1/v_1 , ω_2/v_2 , and ω_3/v_3 ratios are the Miller indices of an arbitrary direction ω in $\{\mathbf{v}_1, \mathbf{v}_2, \mathbf{v}_3\}$ space.

5. Simulated and Experimental SARIGram for Ni(110)

The simulated SARIC image of an azimuthal equidistant projection of He scattering from Ni(110) in Figure 6 was obtained by collecting the scattered He atoms on a virtual hemispherical detector centered over the sample. The contour plot is an azimuthal equidistant projection of the spatial intensity distribution onto the plane of the hemisphere base with angular coordinate equal to the crystal azimuthal angle δ and radial coordinate equal to the polar exit angle β . The experimental SARIS scattering intensity distributions collected for different MCP orientations were mapped to the imaginary hemisphere and then also projected onto the base, corresponding to one quadrant of the azimuthal equidistant projection. The features observed on the map represent an experimental azimuthal equidistant projection that can be directly associated with crystallographic directions characteristic for an fcc (110) surface such as Ni(110). The image areas of low intensity correspond

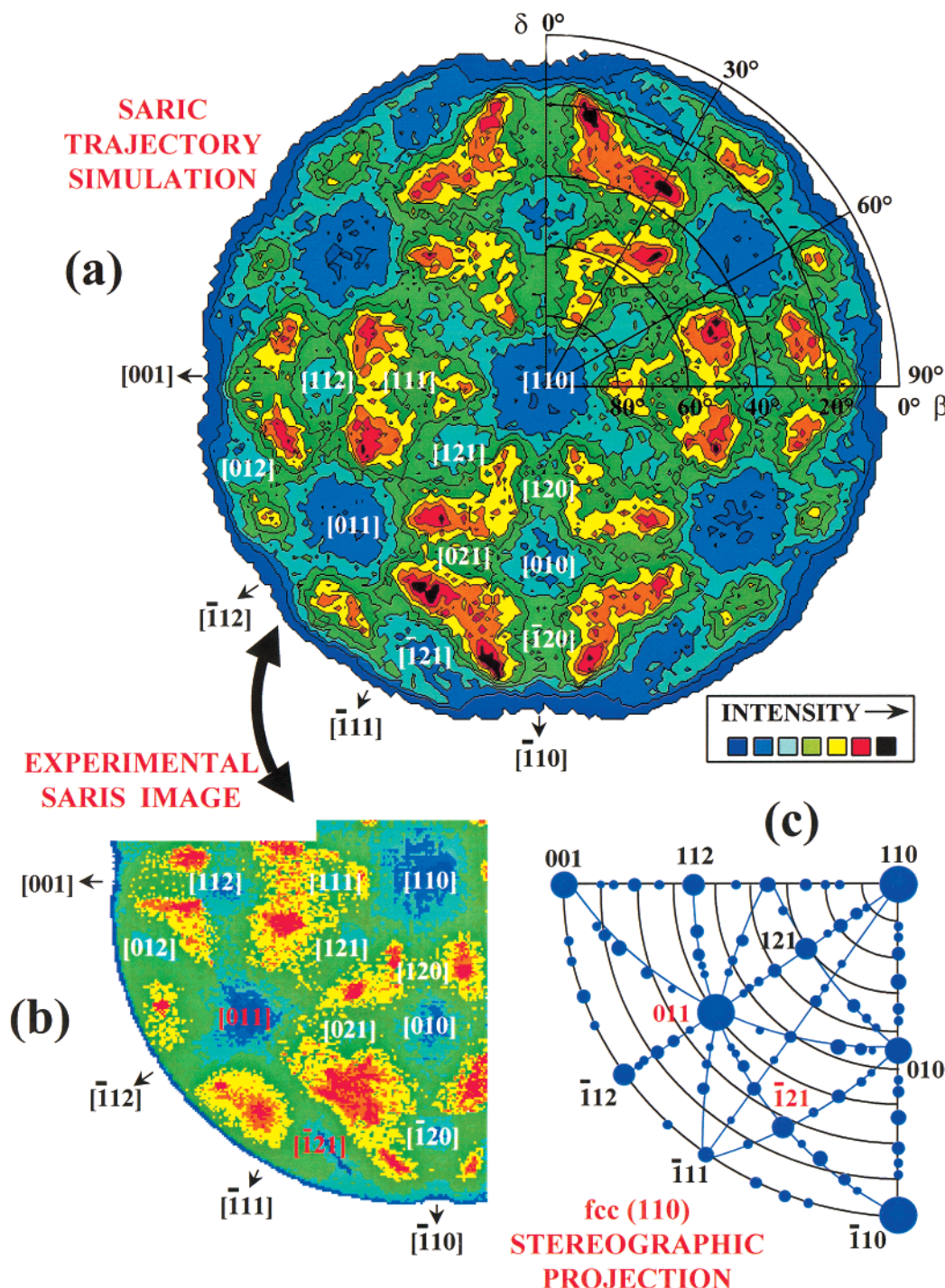


Figure 6. (a) SARIC trajectory simulation of the stereographic projection of 4 keV He^+ scattering from a Ni(110) surface, (b) experimental SARIS image corresponding to one quadrant of the simulation, and (c) a standard fcc (110) stereographic projection.

to blocking cones, the sizes of which are directly related to the angular size of the cone. The agreement of the experimental SARIS image with the standard fcc (110) stereographic projection confirms previous studies⁴² that have found the clean Ni(110) surface is unreconstructed.

6. Termination Layer of CdS(0001)

Examples of SARIS images are shown in Figure 7 for 4 keV Kr^+ ions incident along the $\langle \bar{1}010 \rangle$ azimuth of CdS(0001).³⁴ Time frames corresponding to specific scattering and recoiling events can be identified from the binary collision approximation. The time sequence of these events is the same as that of Figure

3, although the time scales are different because of the different flight path lengths for both experiments. For each frame, the ordinate represents the particle exit angles (β) from the surface, and the abscissa represents the crystal azimuthal angles (δ), i.e., an image in $\{\beta, \delta\}$ space. This is most easily visualized from Figure 4 by assuming yourself to be sitting on the sample surface, facing the detector, and viewing the trajectories as they leave the surface. Because $>95\%$ of these scattered and recoiled particles are neutral,⁴³ we use the term “atoms” instead of “ions”; the detector has equal sensitivity to both of these types of particles when their energies are >1 keV. Each frame of Figure 7 represents the velocity-resolved spatial distribution of particles

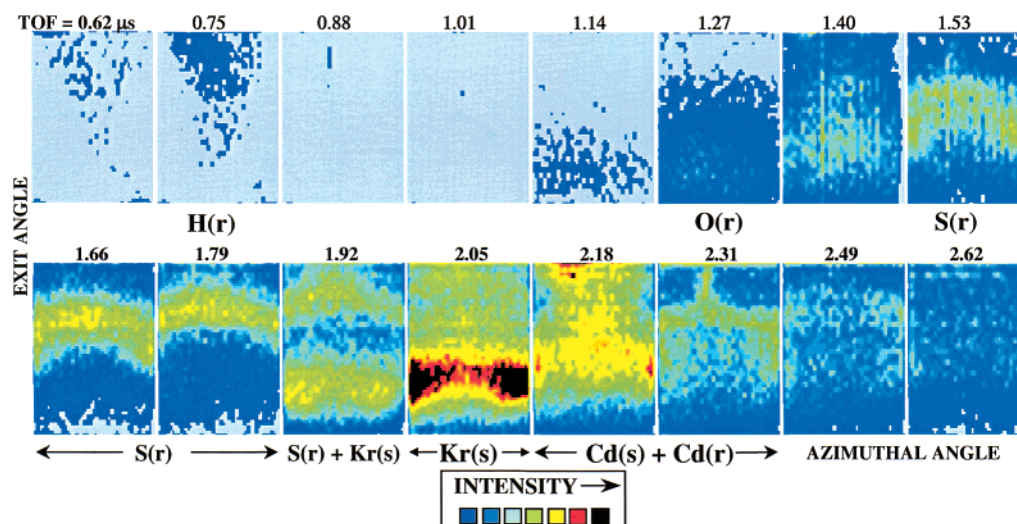


Figure 7. Selected consecutive 16.7 ns SARIS frames for 4 keV Kr^+ scattering from $\text{CdS}(0001)$ with the beam aligned along the $\langle\bar{1}010\rangle$ azimuth. The flight times corresponding to each consecutive image are shown above the frames. Labels corresponding to the dominant scattering, $\text{Kr}(s)$, and recoiling, $\text{H}(r)$, $\text{O}(r)$, and $\text{S}(r)$, events are listed below their respective frames.

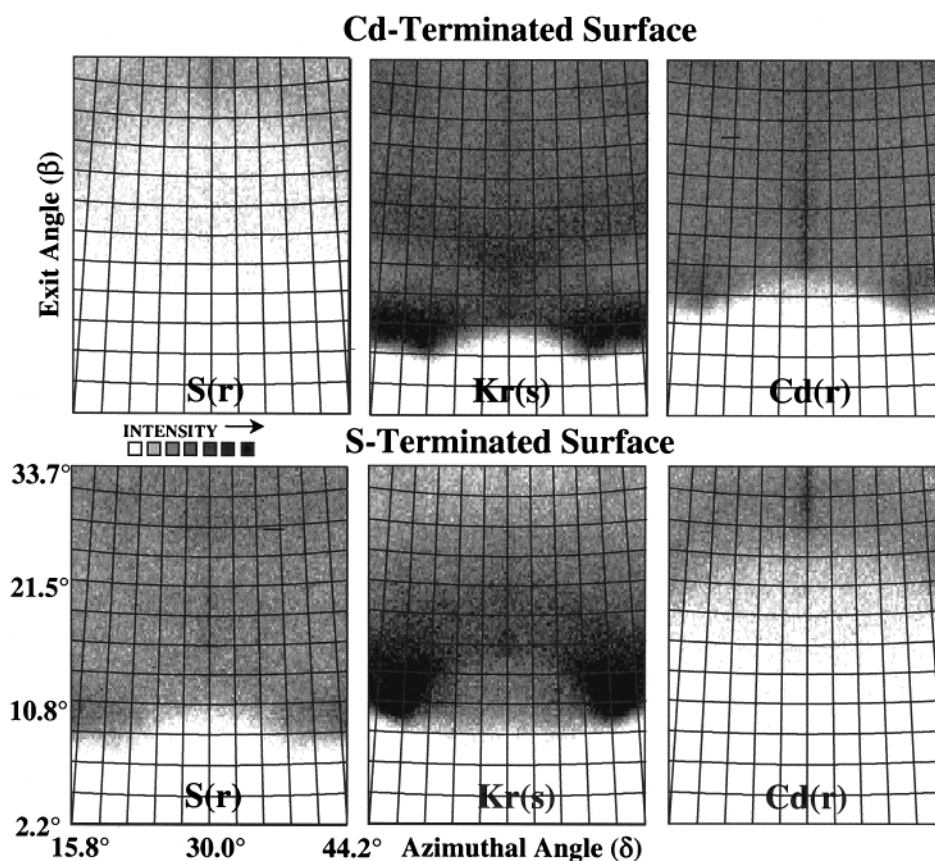


Figure 8. Simulated images from the SARIC program for both the Cd- and S-terminated $\text{CdS}(0001)$ surfaces using the same conditions as the experimental images of Figure 7. Separate images are shown for Kr scattered from Cd atoms [$\text{Kr}(s)/\text{Cd}$] and for recoiled Cd atoms [$\text{Cd}(r)$] and S atoms [$\text{S}(r)$]. These images are not time-resolved; therefore, the $\text{Kr}(s)/\text{Cd}$ image contains both QSS and MS Kr atoms.

arriving at the MCP in consecutive 16.7 ns windows. These consecutive frames resolve the different spatial distributions for scattered Kr and recoiled Cd, S, H, and O atoms.

The images are symmetrical about the $\langle\bar{1}010\rangle$ azimuth, as is the crystal structure. The spatial distribution of the scattered Kr signal appears as two intense spots at the edges of the 2.05 μs frame at a low exit angle of $\beta \sim 9^\circ$ and at azimuthal positions of $\delta \sim \pm 8^\circ$; this frame corresponds to the single scattering (SS) of Kr from Cd. The 2.18 and 2.31 μs frames correspond to

slower particles and exhibit additional features at higher exit angles. These images exhibit a horizontal streak of intensity in the $\beta \sim 17^\circ\text{--}26^\circ$ range, which is considerably higher than that of SS Kr at 2.05 μs ; this streak corresponds to multiply scattered Kr. The vertical streak of intensity observed in both of these frames that is centered along the symmetrical azimuth at high β is due to recoiling of Cd atoms. This focusing arises from the recoiling of Cd atoms from the second bilayer and a focusing along the outgoing trajectory by first-bilayer Cd and S atoms.

Note that this vertical streak is $\sim 2^\circ$ off the symmetrical position because of a slight misalignment of the azimuthal angle.

Structure analyses can be obtained from these images by using SARIC simulations as a function of the surface structure parameters. Examples of SARIC images for both the Cd- and the S-terminated surfaces of CdS using bulk interatomic spacings and bond angles are shown in Figure 8. Both scattering from and recoiling of first-layer atoms occurs at lower exit angles β than similar processes from second-layer atoms. Trajectories from second-layer atoms require higher β values to escape from the surface. A comparison of the images in Figures 7 and 8 shows that there is agreement only with the simulated images of the Cd-terminated surface and not with those of the S-terminated surface. For the simulated images of the Cd-terminated surface, the two low- β peaks for scattered Kr(s)/Cd are at $\beta \sim 9^\circ$ (Figure 8), in agreement with the 2.05 μs frame of Figure 7. The arch for recoiled S(r) atoms exhibits a maximum near $\beta \sim 30^\circ$ (Figure 8), as observed in the 1.66 and 1.79 μs frames of Figure 7. Simulations for the S-terminated surface in Figure 8 yield the two scattered Kr(s)/Cd peaks at $\beta \sim 13^\circ$ and the recoiled S(r) arch maximum near $\beta \sim 14^\circ$, in disagreement with the respective frames of Figure 7. This shows that SARIS is sensitive to and capable of identifying the outermost termination layer of a surface.

7. Chemisorption Site of Cl on Ni(110)

SARIS images of 4 keV Ar^+ ions scattering from clean Ni(110), and this surface after exposure to Cl_2 gas, are shown in Figure 9a. Each frame represents the velocity-resolved spatial distributions of Ar atoms scattering along the $\langle \bar{1}10 \rangle$ azimuth and arriving at the MCP in windows of 16.7 ns duration. The selected window at 1.4 μs corresponds to the flight time of quasi-single-scattered Ar atoms from the Ni sample to the MCP. The images of Figure 9a are symmetrical about the $\langle \bar{1}10 \rangle$ azimuth, as is the crystal structure. This is in accord with our low-energy electron diffraction (LEED) measurements that exhibit a (1×1) pattern for clean Ni and a (3×1) pattern for Cl/Ni. The differences in these images, i.e., $[(\text{Cl}/\text{Ni}) - (\text{clean Ni})]$, clearly reveal regions of altered intensities due to the presence of Cl atoms. A combination of the difference images along $\langle \bar{1}10 \rangle$ and 15° off the azimuth, which spans a broader azimuthal range, reveals intensification (focusing) of trajectories along $\langle \bar{1}10 \rangle$ and blocking for angles on either side of this azimuthal direction.

There are three chemically active symmetrical sites on the Ni(110)- (3×1) surface, as shown in Figure 9b: SB, short-bridge site between two first-layer Ni atoms along $\langle \bar{1}10 \rangle$; LB, long-bridge site between two first-layer Ni atoms along $\langle 001 \rangle$; and H, 4-fold hollow site between four first-layer Ni atoms. SARIC simulations were performed with Cl at each of these sites and at different heights above the surface. A two-dimensional reliability,³³ or R , factor, based on the differences between the experimental and simulated images, was calculated as a function of Cl atom height above the surface. A minimum in R was obtained for the SB position with the Cl atoms 1.9 ± 0.1 Å above the Ni rows, corresponding to a Cl–Ni bond length of 2.3 ± 0.1 Å; the sensitivity of R to changes in the Cl height is $\sim 5\%$ for a 0.1 Å change. The bond length⁴⁴ for Cl bridge-bonded to two Ni atoms is 2.45 Å, confirming dissociative chemisorption and bonding of Cl atoms to Ni atoms. Previous STM work⁴⁵ on this system is in agreement with this assignment, showing that Cl_2 chemisorbs dissociatively on Ni(110) and forms atom pairs oriented along the $[001]$ direction, with the Cl–Cl spacings comparable to the bulk Ni lattice constant.

The (3×1) LEED pattern can be obtained from two different types of structures, i.e., single rows of Cl atoms or single missing

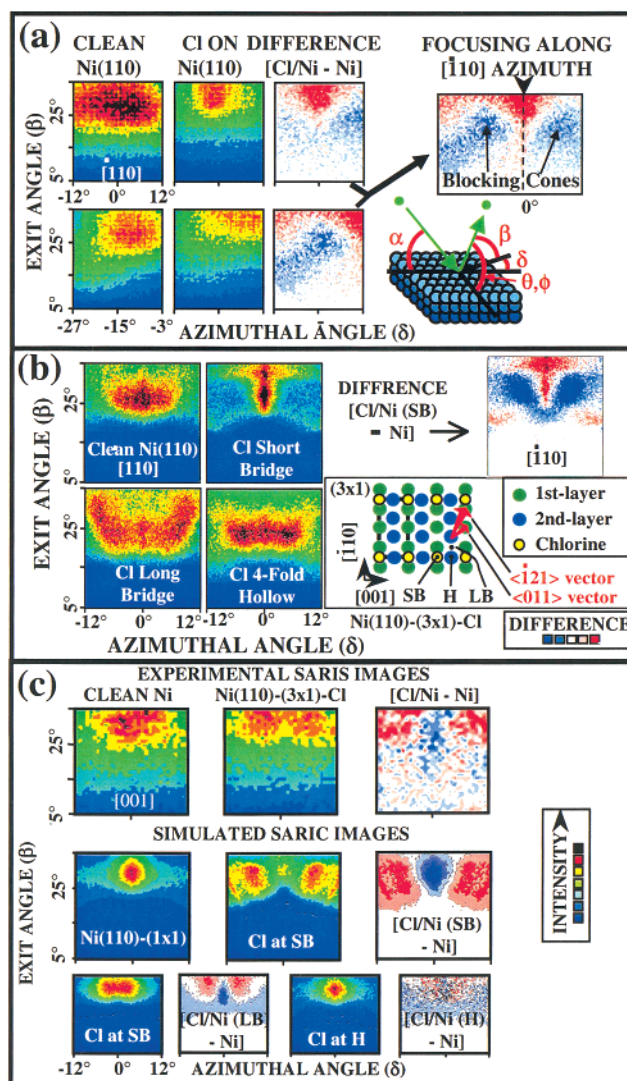


Figure 9. (a) SARIS images of 4 keV Ar^+ scattering from Ni(110)- (1×1) and Ni(110)- (3×1) -Cl along $\langle \bar{1}10 \rangle$ (top) and 15° off this azimuth (bottom). The difference image reveals focusing of scattered Ar trajectories in the centers of the $\langle \bar{1}10 \rangle$ troughs. (b) SARIC simulations of 4 keV Ar^+ scattering from Ni(110)- (1×1) and Ni(110)- (3×1) -Cl with Cl in the short-bridge (SB), long-bridge (LB), and 4-fold-hollow (H) sites. The SB site provides the best agreement with the experimental images of part a. The interatomic vectors highlighted in red in Figure 6 (b and c). (c) SARIS images and SARIC simulations of Ni atoms recoiled by 4 keV Kr^+ along the $\langle 001 \rangle$ azimuth from Ni(110)- (1×1) and Ni(110)- (3×1) -Cl.

rows of Cl atoms along $\langle 001 \rangle$ that repeat every third SB position. Recoil of Ni atoms along the $\langle 001 \rangle$ azimuth is highly sensitive to these two different coverages because of deflection of Ni atoms by Cl atoms along this direction. Ni atoms recoiled by Kr projectiles are resolved in the 2.7 μs window shown in Figure 9c. Excellent agreement is obtained between experimental and simulated images for single rows of Cl atoms at the SB site; the other sites provide poor agreement, in accord with the scattered Ar results of Figure 9a and b. The perturbations by the Cl atoms on the recoiled Kr trajectories can be deciphered from simulated trajectories. Along $\langle 001 \rangle$, the Cl atoms are not situated along adjacent sides of a single deep trough where they can enhance focusing of trajectories. Instead, they deflect the Ni recoil trajectories, resulting in a decrease in intensity along $\langle 001 \rangle$, as shown in Figure 9c.

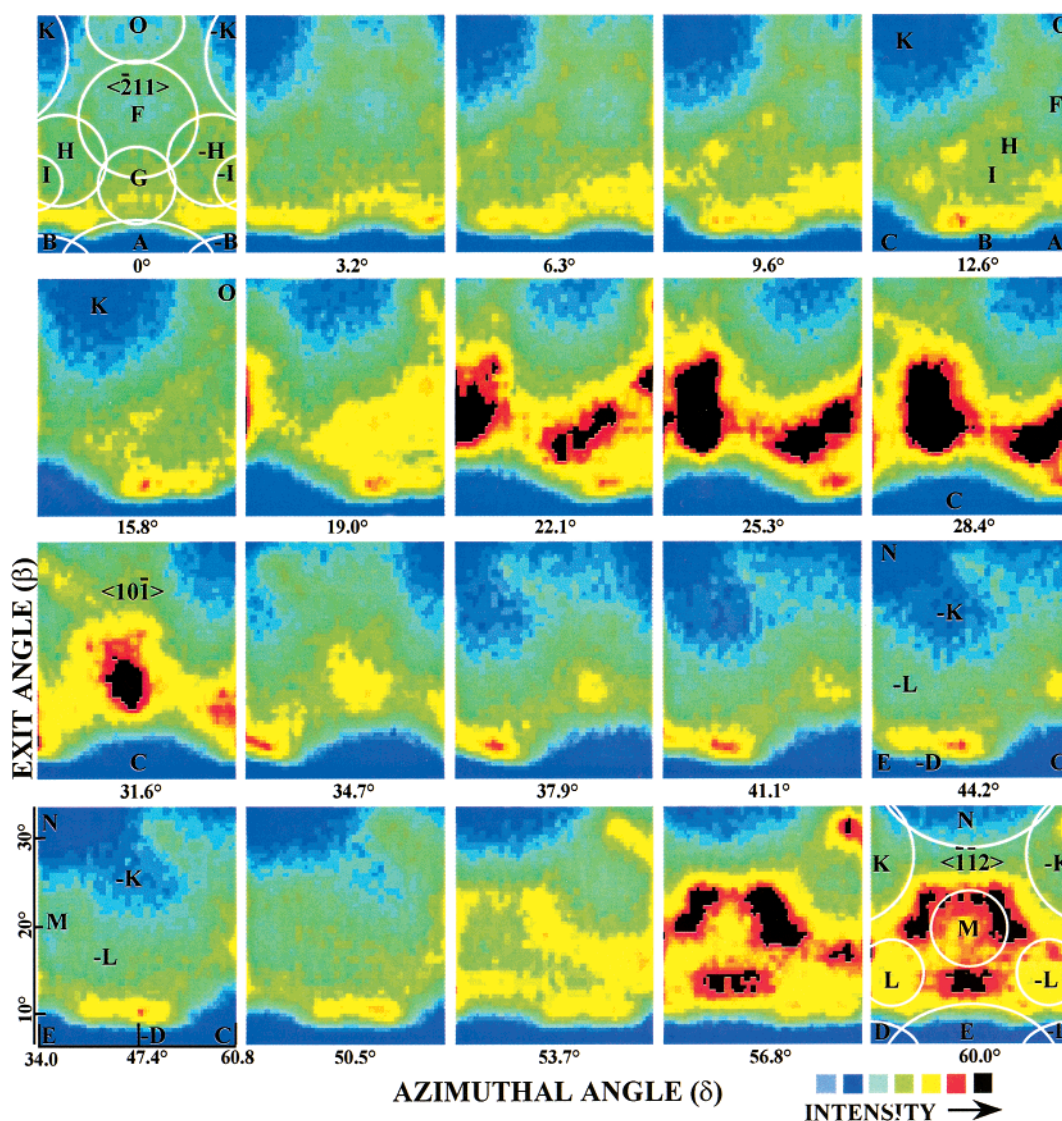


Figure 10. Series of 20 time-resolved SARIS frames for 4 keV He⁺ scattering from Pt(111)-(1 × 1) taken every 3° of rotation about the azimuthal angle δ , starting with the $\langle 211 \rangle$ azimuth at $\delta = 0^\circ$ and ending with the $\langle \bar{1}\bar{1}2 \rangle$ azimuth at $\delta = 60^\circ$. Each frame represents a 16.7 ns window centered at the TOF corresponding to quasi-single scattering as predicted by the binary collision approximation. The white circles on the $\delta = 0^\circ$ and 60° frames represent the positions and relative sizes of calculated blocking cones.

8. Quantative Analysis of the Pt{111} Surface

A series of time-resolved He scattering images⁴⁶ taken as a function of azimuthal angle δ are shown in Figure 10. The crystal was rotated about its surface normal by 3° for each image. Each image is taken from a 16.7 ns frame corresponding to the SS TOF. The observed images are rich in features that change in position and intensity as a function of azimuthal angle. The regions of low intensity correspond to the positions of the centers of the blocking cones; these regions have circular or oval shapes with distortions caused by other overlapping blocking cones. The regions of high intensity correspond to the positions of intersection or near overlap of blocking cones; atom trajectories are highly focused along the edges of the cones.

The images at $\delta = 0^\circ$ and 60° along the $\langle 211 \rangle$ and $\langle \bar{1}\bar{1}2 \rangle$ azimuths, respectively, are symmetrical about a vertical line through the center of the frame, as is the crystal structure along these azimuths, as shown in Figure 11a. The shifts in the positions and sizes of the blocking cones can be monitored as δ is rotated away from the 0° or 60° direction. There are large variations in the intensities as a function of δ , with the highest intensities being observed along the directions $\delta = 22\text{--}32^\circ$ and

$56\text{--}60^\circ$. These features result from the focusing of ions onto second-layer atoms by the shadow cones of first-layer atoms. The second-layer atoms are in sites that are asymmetrical with respect to the first layer, resulting in nonplanar scattering trajectories. Intense features in asymmetrical positions are observed at higher exit angles. These features correspond to semichanneling⁴⁷ in asymmetrical channels. Semichannels are “valleys” in surfaces through which scattered ions are guided. Along the $\langle 101 \rangle$ direction, the first-layer atoms form the “walls”, and the second-layer atoms form the “floor” of the semichannel. However, the second-layer rows are not centered in the bottom of the channel, resulting in an asymmetrical channel. As a result, the scattered atom trajectories are bent and focused along directions determined by the asymmetry of the channel.

The frames along the 0° $\langle 211 \rangle$ and 60° $\langle \bar{1}\bar{1}2 \rangle$ azimuths in Figure 10 were selected to compare with those of blocking cone analyses and ion trajectory simulations. The arrangement of the first-layer atoms is identical along both of these azimuths; however, the second- and third-layer atoms have a different arrangement with respect to the first-layer atoms, as shown in Figure 11a. He atoms scattered from second- and third-layer

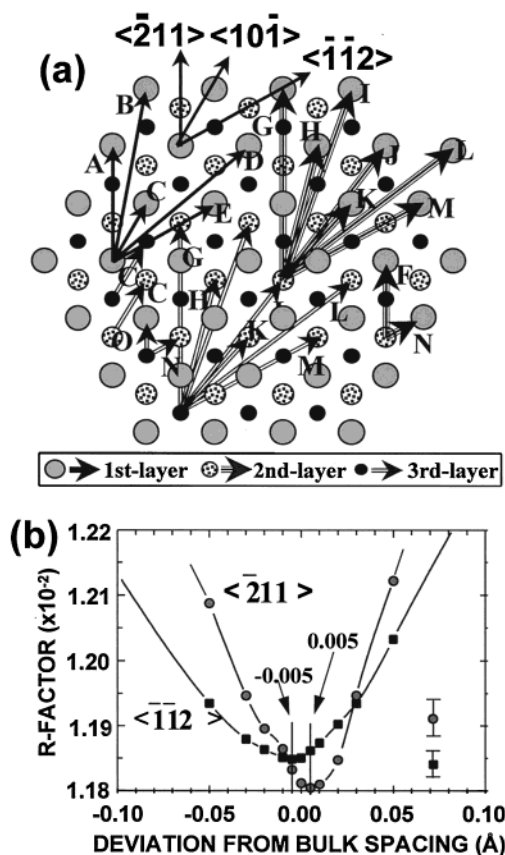


Figure 11. (a) Schematic drawing of the Pt{111}-(1 × 1) surface. Arrows indicate the nearest neighbor first-first-, second-first-, and third-first-layer interatomic vectors. (b) Two-dimensional R factors as a function of the deviation (d) of the first-second interlayer spacing from the bulk value. The experimental and simulated images along the $\langle 211 \rangle$ and $\langle 112 \rangle$ azimuths of Figure 12 were used in the comparison.

atoms experience a different arrangement of blocking cones on their exit from the surface. The positions of the blocking cones were calculated from the projections of the interatomic vectors onto the MCP detector (Figure 11a). The critical blocking angles or sizes of the cones were calculated from SARIC. The results are shown in Figure 12. The blocking of scattering trajectories from n th-layer atoms by their neighboring n th-layer atoms is observed at low β because these atoms are all in the same plane. This first-layer atom-first-layer atom blocking contributes most of the intensity at low β . The arcs corresponding to the edges of the blocking cones (Figure 12), resulting from the vectors **A**, **B**, **D**, and **E** in Figure 11, occur at $\beta \sim 10^\circ$. The features at higher β correspond to scattering trajectories from second- and third-layer atoms that are blocked and focused by first-layer atoms. The cones resulting from the vectors **F**, **G**, and **O** along the azimuthal direction $\langle 211 \rangle$ and **M** and **N** along $\langle 112 \rangle$ are due to scattering trajectories from second- and third-layer atoms that are blocked by first-layer atoms along these symmetrical directions. These are centered along the azimuths and are directed to higher β values for shorter interatomic spacings. Blocking cones due to the vectors **H**, **I**, **K**, and **L** result from second- and third-layer scattering and are observed at δ values off of the 0° and 60° directions because of nonplanar scattering trajectories.

Quantitative analyses can be achieved by using the SARIC simulation and minimization of the R factor³² between the experimental and simulated images as a function of the structural parameters. SARIC was used to generate simulated images of 4 keV He⁺ scattering from bulk-terminated Pt{111} as a

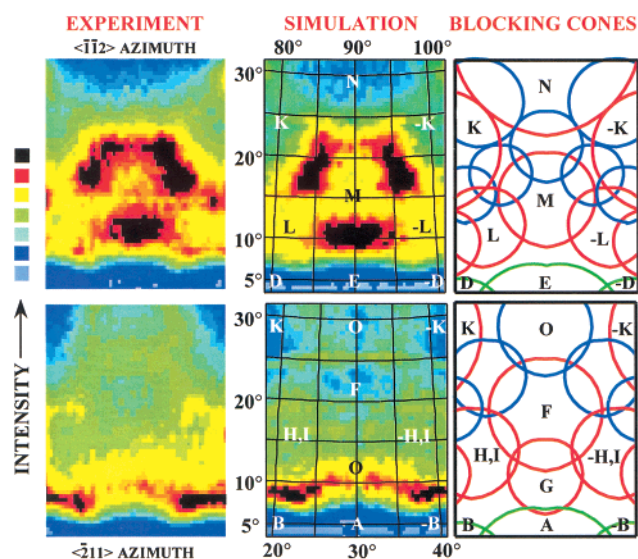


Figure 12. Experimental SARIS images (left), simulated SARIC images (center), and blocking cone analysis (right) for He⁺ scattering along the $\langle 211 \rangle$ and $\langle 112 \rangle$ azimuths of Pt(111). For the calculated blocking cones, first-first, first-second, and first-third layer interactions are identified by green, red, and blue lines, respectively. The letters correspond to the interatomic vectors identified in Figure 11a.

function of the first-second interlayer spacing d . Isotropic thermal vibrations with an amplitude of 0.1 Å were included in the model. A two-dimensional reliability, or R , factor, based on the differences between the experimental and simulated patterns, was calculated as a function of the deviation d of the first-second interlayer spacing from the bulk value. The plots shown in Figure 11b exhibit minima at $\Delta d_{\min} = -0.005$ and $+0.005$ Å for the $\langle 112 \rangle$ and $\langle 211 \rangle$ azimuths, respectively. The optimized simulated images corresponding to d_{\min} are shown in Figure 12; there is good agreement between these simulated and experimental images. The R factors are sensitive to changes in the interlayer spacing at the level of 0.01 Å. On the basis of these data, we conclude that the Pt{111} surface is bulk-terminated with the first-second layer spacing within ± 0.01 Å, or 0.4%, of the 2.265 Å bulk spacing. This sensitivity is less than the uncertainty due to the thermal vibrations because SARIS samples the average positions of lattice atoms.

9. Direct Detection of Hydrogen Atoms on Pt(111)

Although the presence of hydrogen atoms on a surface is generally considered to present only a minor perturbation on the scattering trajectories of heavy atoms, recent low-keV channeling measurements^{37,38} using TOF-SARS have shown that the hydrogen atoms can perturb the trajectories of heavier projectiles such as Ne to a detectable level. Such low-energy ion channeling measurements are capable of probing the positions of light elements on heavy substrates with analysis by simple geometrical constructs. Examples of SARIGrams⁴⁸ for 5 keV Ne⁺ scattered from the clean Pt(111) and Pt(111)-(1 × 1)-H surfaces are shown in Figure 13.

9.1. Clean Pt(111). For the clean Pt surface, sharp intense features with an apparent 60° periodicity that correspond to focusing of the scattered projectiles by "atomic lenses" of the crystal surface are observed. These intense features are separated from one another by low-intensity regions that originate from blocking cones situated along the exit trajectories of the scattered Ne atoms. Specifically, for this angular configuration, the low-intensity regions are due to the superposition of blocking cones centered at $\beta = 0^\circ$ formed by scattered trajectories from first-

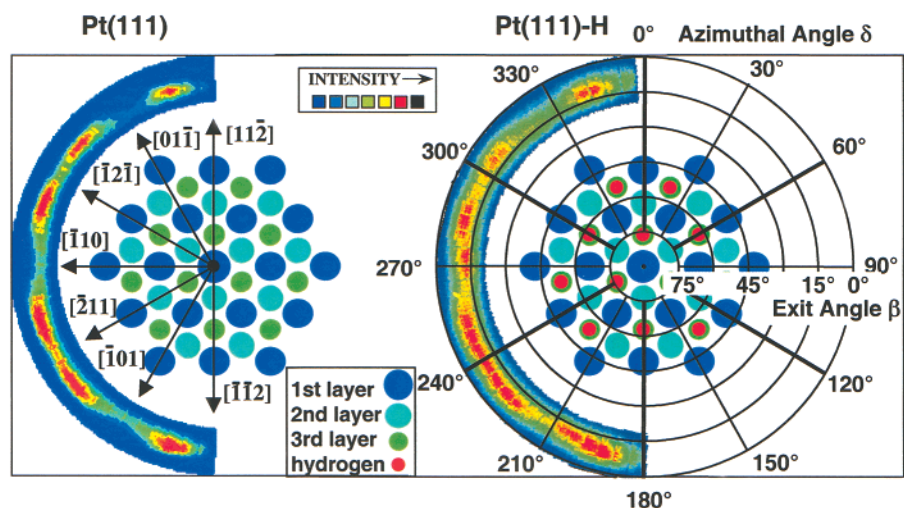


Figure 13. SARIgrams for 5 keV Ne^+ scattering from Pt(111) and Pt(111)-(1 \times 1)-H surfaces. The SARIgrams were constructed by using an azimuthal equidistant projection of 32 individual SARIS images. Incident angle, $\alpha = 19^\circ$; scattering angle to detector normal, $\theta = 24^\circ$; and flight path to detector center, 17 cm.

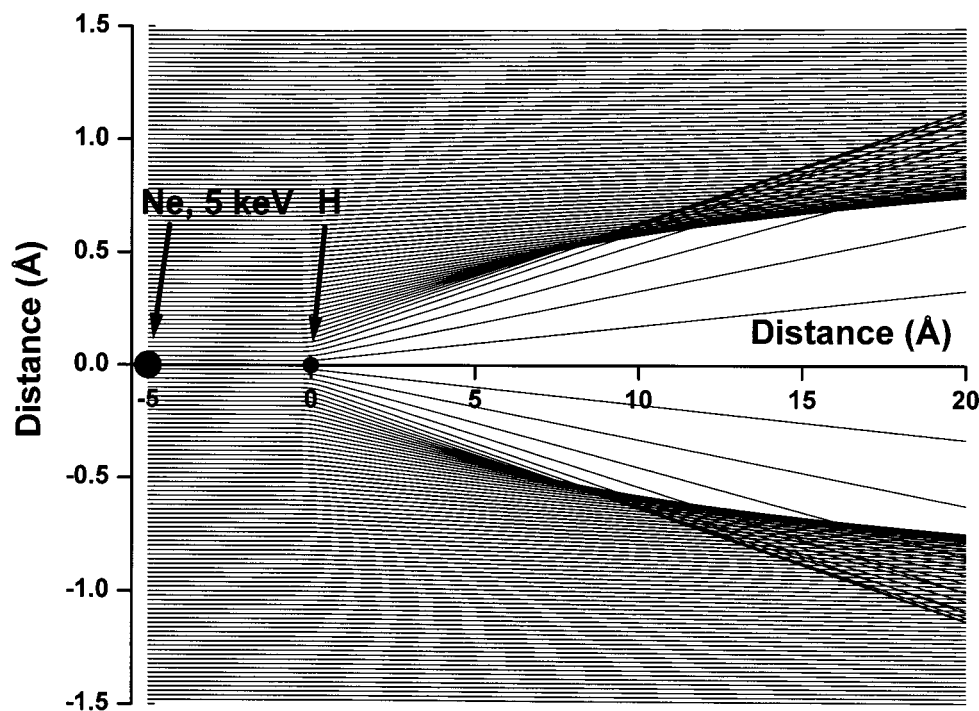


Figure 14. A flux of parallel 5 keV Ne atom trajectories impinging on a H atom with impact parameters p that are incremented by 0.02 Å.

layer atoms that are blocked by neighboring first-layer atoms as well as cones centered at $\beta > 0^\circ$ resulting from scattering from subsurface atoms and blocking by first-layer atoms. Each of the crystallographic directions indicated on the SARIgram in conjunction with the [111] crystal direction defines a plane of symmetry that bisects the corresponding blocking feature, i.e., the feature is symmetrical about these azimuths. It is observed that the recorded resultant blocking is most pronounced at the [011], [110], and [101] azimuths and appears as only small indentations at the [121] and [211] azimuths. The angular positions of these three dominant blocking features suggest a 6-fold symmetry because they result from only first-layer scattering. Scattering with a higher incidence angle allows sampling of subsurface layers and reveals the 3-fold symmetry of the (111) surface.

9.2. Pt(111)-(1 \times 1)-H. The SARIgram of the hydrogen-covered Pt(111) surface exhibits basic features similar to those

of the clean surface, although severely broadened. It is clear that the aforementioned blocking features are attenuated to different extents. After hydrogen adsorption, the intensity gradients, i.e., $[\partial I(\delta, \beta)/\partial \delta]_{7^\circ < \beta < 15^\circ}$, at the azimuthal directions 240° and 300° almost vanish. At the azimuthal directions 210° , 270° , and 330° , these gradients remain large and recognizable, although the features at 270° do not remain as clear as those at 210° and 330° . The reason for the different features at 270° is still not clear. This could be caused by H atoms occupying both fcc and hcp sites at this coverage or by small displacements of the Pt atoms as a result of chemisorption. These observations are in accord with the fact that the H atoms on the surface are capable of deflecting the Ne trajectories by a maximum of $\sim 3^\circ$, which amounts to a deflection of ~ 9 mm on the MCP under the experimental configuration. Accordingly, the two small indentations at the [121] and [211] azimuths vanish completely.

The scattering of Ne atoms by H atoms can be better understood by considering the actual trajectories of the colliding atoms. Figure 14 shows a flux of parallel 5 keV Ne atom trajectories impinging on a H atom. For the H/Ne case where $M_t/M_p < 1$, some small p collisions result in penetration of the cone by the projectile atom M_p , although a distinct focusing of large p trajectories exists, resulting in a "semi-transparent cone". Such semi-transparent cones have also been observed^{49,50} for hydrogen chemisorbed on a tungsten surface. For $p = 0$, the projectile atoms M_p follow the target atoms M_t through the center of the cone.

The importance of the SARIGram of the hydrogen exposed surface is 3-fold. (1) It demonstrates that H atoms are capable of deflecting Ne atom trajectories and that this deflection can be directly observed. (2) The delocalization of intensities on the SARIGram after hydrogen adsorption infers an increase in the number of scatters per unit cell. (3) The sensitivity to local atomic arrangements provides a direct probe of the chemically active sites for hydrogen adsorption.

9.3. Interpretation of SARIGrams. The changes in the shapes and intensities of the blocking features in the SARIGrams of Figure 13 as a result of exposure to hydrogen are a manifestation of (1) the different geometrical interceptions of the respective blocking cones on the detector surface and (2) the proximity of the H atoms to the Ne trajectories. Hydrogen atoms adsorbed at the fcc sites are contained in the planes defined by the [111] and the $[\bar{1}2\bar{1}]$ or $[\bar{2}11]$ crystal directions and situated 0.9 Å above the surface plane in the fcc sites, as found previously.⁵¹ Therefore, they can directly perturb the incoming and outgoing Ne trajectories along these azimuths. This defocusing by the H atoms results in the large changes observed in Figure 13 along 240° and 300° in the SARIGram of the hydrogen-exposed surface. The features along 210°, 270°, and 330° remain salient after exposure to hydrogen because most of the Ne trajectories scattering along these directions do not make direct collisions with H atoms.

The large p collisions result in significant deflections of the incoming Ne beam such that the scattered Ne trajectories exhibit large deviations from the focused beams of the clean surface. Because these large p collisions occur with the highest probability, these types of trajectories are the dominant contributors to the broadening observed as a result of hydrogen chemisorption. Similar features can be observed along the $[\bar{2}11]$ azimuth. These specific data, however, do not distinguish between chemisorption at the fcc or hcp sites. Low-energy ion channeling experiments provide this distinction.^{37,38,48}

10. Summary

A battery of surface analysis techniques has been developed for studying the composition and structure of the surface layers of materials. These techniques have been invaluable in advancing the field of surface science. As trends in microelectronic devices move toward smaller, more densely packed components, it is necessary to develop new methods for analysis and fabrication of nanometer-scale structures. The composition and atomic structures of these ordered surfaces, the immediate subsurface layers, and adsorbates (especially hydrogen) on these surfaces remain problematic for many systems. Low-energy ion scattering has now been well-established as an extremely surface-sensitive technique for determining the composition and structure of surfaces. Dynamic surface processes such as chemical reactions, reconstruction, relaxation, diffusion, and film growth often involve the transport of large numbers of atoms, e. g., reconstruction of a surface layer can involve the rear-

angement of $>10^{15}$ atoms/cm². A technique that can provide direct element-specific surface atomic structural information at a subangstrom level and a short time scale that can be unambiguously interpreted is needed for probing surface composition and structure and mechanisms of dynamic processes. SARIS is being developed with these objectives in mind.

Acknowledgment. This material is based on work supported by the National Science Foundation under Grant 9986807 and the R. A. Welch Foundation under Grant E-656.

References and Notes

- (1) Morrison, S. R. *The Chemical Physics of Surfaces*, 2nd ed.; Plenum Press: New York, 1990.
- (2) *Surface Science: The First Thirty Years*; Duke, C., Ed.; North-Holland, Amsterdam, 1994.
- (3) Smith, D. P. *J. Appl. Phys.* **1967**, *38*, 340.
- (4) Heiland, W.; Taglauer, E. *Surf. Sci.* **1977**, *68*, 96; **1975**, *47*, 234; *Radiat. Eff. Defects Solids* **1973**, *19*, 1. Heiland, W.; Iberl, F.; Taglauer, E.; Menzel, D. *Surf. Sci.* **1975**, *53*, 383.
- (5) Brongersma, H. H.; Theeten, J. B. *Surf. Sci.* **1976**, *54*, 519. Brongersma, H. H.; Mul, P. *Surf. Sci.* **1973**, *35*, 393.
- (6) Suurmijer, E. P. Th. M.; Boers, A. L. *Surf. Sci.* **1973**, *43*, 309.
- (7) DeWit, A. G. J.; Bronckers, R. P. N.; Fluit, J. M. *Surf. Sci.* **1979**, *82*, 177.
- (8) Aono, M.; Hou, Y.; Souda, R.; Oshima, C.; Otani, S.; Ishizawa, Y.; Matsuda, K.; Shimizu, R. *Jpn. J. Appl. Phys.* **1982**, *21*, L670. Aono, M.; Hou, Y.; Oshima, C.; Ishizawa, Y. *Phys. Rev. Lett.* **1982**, *49*, 567. Aono, M.; Souda, R. *Jpn. J. Appl. Phys.* **1985**, *24*, 1249.
- (9) Spitzl, R.; Niehus, H.; Comsa, G. *Surf. Sci.* **1991**, *250*, L355.
- (10) Herman, G. S. *Phys. Rev. B* **1999**, *59*, 14899.
- (11) Cornelison, D. M.; Worthington, M. S.; Tsong, I. S. T. *Phys. Rev. B* **1990**, *46*, 4051.
- (12) Overbury, S. H.; van den Oetelaar, R. J. A.; Zehner, D. M. *Phys. Rev. B* **1993**, *48*, 1718.
- (13) Yarmoff, J. A.; Cyr, D. M.; Huang, J. H.; Kim, S.; Williams, R. S. *Phys. Rev. B* **1986**, *33*, 3856.
- (14) Umezawa, K.; Nakanishi, S.; Gibson, W. M. *Surf. Sci.* **1999**, *426*, 225.
- (15) Mintz, M. H.; Atzmony, U.; Shamir, N. *Surf. Sci.* **1987**, *185*, 413.
- (16) Xu, C.; O'Connor, D. J. *Nucl. Instrum. Methods Phys. Res. B* **1991**, *53*, 315.
- (17) Lu, H. C.; Gusev, E. P.; Garfunkel, E.; Gustafsson, T. *Surf. Sci.* **1996**, *351*, 111.
- (18) Daley, R. S.; Farrelly, D.; Williams, R. S. *Surf. Sci.* **1990**, *234*, 355.
- (19) Marchut, L.; Buck, T. M.; Wheatley, G. H.; McMahon, C. J., Jr. *Surf. Sci.* **1984**, *141*, 549.
- (20) Rabalais, J. W. *Science* **1990**, *250*, 521.
- (21) Grizzi, O.; Shi, M.; Bu, H.; Rabalais, J. W. *Rev. Sci. Instrum.* **1990**, *61*, 740.
- (22) Kim, C.; Höfner, C.; Al-Bayati, A.; Rabalais, J. W. *Rev. Sci. Instrum.* **1998**, *69*, 1676. Yao, J.; Kim, C.; Rabalais, J. W. *Rev. Sci. Instrum.* **1998**, *69*, 306. Kim, C.; Al-Bayati, A.; Rabalais, J. W. *Rev. Sci. Instrum.* **1998**, *69*, 1289.
- (23) Mashkova, E. S.; Molchanov, V. A. *Medium-Energy Ion Reflection From Solids*; North-Holland: Amsterdam, 1985.
- (24) Parilis, E. S.; Kishinevsky, L. M.; Turaev, N. Yu.; Baklitzky, B. E.; Umarov, F. F.; Verleger, V. Kh.; Bitensky, I. S. *Atomic Collisions on Solids*; North-Holland: New York, 1993.
- (25) Zeigler, J. F.; Biersack, J. P.; Littmark, U. *The Stopping and Range of Ions in Solids*; Ziegler, J. F., Ed.; Pergamon Press: New York, 1985.
- (26) Rabalais, J. W. *Crit. Rev. Solid State Mater. Sci.* **1988**, *14*, 319.
- (27) Poole, R. *Science* **1989**, *246*, 995.
- (28) Goldstein, H. *Classical Mechanics*, 2nd ed.; Addison-Wesley: Reading, MA, 1980.
- (29) Rabalais, J. W. *Surf. Sci.* **1994**, *299/300*, 219.
- (30) Bykov, V.; Kim, C.; Sung, M. M.; Boyd, K. J.; Todorov, S. S.; Rabalais, J. W. *Nucl. Instrum. Methods Phys. Res. B* **1996**, *114*, 371.
- (31) Sung, M. M.; Bykov, V.; Al-Bayati, A.; Kim, C.; Todorov, S. S.; Rabalais, J. W. *Scanning Microsc.* **1995**, *9*, 321.
- (32) Kim, C.; Höfner, C.; Rabalais, J. W. *Surf. Sci.* **1997**, *388*, L1085.
- (33) Höfner, C.; Bykov, V.; Rabalais, J. W. *Surf. Sci.* **1997**, *393*, 184.
- (34) Kim, C.; Ahn, J.; Bykov, V.; Rabalais, J. W. *Int. J. Mass Spectrom. Ion Phys.* **1998**, *174*, 305.
- (35) Höfner, C.; Rabalais, J. W. *Phys. Rev. B* **1998**, *58*, 9990.
- (36) Höfner, C.; Rabalais, J. W. *Surf. Sci.* **1998**, *400*, 189.
- (37) Lui, K. M.; Kim, Y.; Lau, W. M.; Rabalais, J. W. *Appl. Phys. Lett.* **1999**, *75*, 587.

- (38) Lui, K. M.; Kim, Y.; Lau, W. M.; Rabalais, J. W. *J. Appl. Phys.* **1999**, in press.
- (39) Houssiau, L.; Rabalais, J. W. *Nucl. Instrum. Methods Phys. Res.* **1999**, *157*, 274.
- (40) Rousseau, J. J. *Basic Crystallography*; Wiley: Chichester, U.K., 1998.
- (41) Robinson, A. H.; Sale, R. D. *Elements of Cartography*, 3rd ed.; Wiley: New York, 1969. Raisz, E. J. *Principles of Cartography*; McGraw-Hill: New York, 1962.
- (42) Watson, P. R.; van Hove, M. A.; Herman, K. K. *Atlas of Surface Structures*; American Chemical Society and American Institute of Physics: Washington, D.C., 1994; Vol. 1A.
- (43) Houssiau, L.; Wolfgang, J.; Nordlander, P.; Rabalais, J. W. *Phys. Rev. Lett.* **1998**, *81*, 5153; *J. Chem. Phys.* **1999**, *110*, 8139.
- (44) Orpen, A.; Brammer, L.; Allen, F. H.; Kennard, O.; Watson, D. G.; Taylor, R. *J. Chem. Soc., Dalton Trans.* **1989**, S1–S83.
- (45) Fishlock, T. W.; Pethica, J. B.; Jones, F. H.; Egddell, R. G.; Foord, J. S. *Surf. Sci.* **1997**, *377*, 629.
- (46) Kim, C.; Rabalais, J. W. *Surf. Sci.* **1997**, *385*, L938.
- (47) Kim, C.; Rabalais, J. W. *Surf. Sci.* **1997**, *395*, 239.
- (48) Lui, K. M.; Kim, Y.; Kim, S. S.; Lau, W. M.; Bykov, V.; Rabalais, J. W. *J. Chem. Phys.* **1999**, *111*, 11095.
- (49) Grizzi, O.; Shi, M.; Bu, H.; Rabalais, J. W.; Hochman, P. *Phys. Rev. B* **1989**, *40*, 10127.
- (50) Shi, M.; Grizzi, O.; Bu, H.; Rabalais, J. W.; Nordlander, P. *Phys. Rev. B* **1989**, *40*, 10163.
- (51) Umezawa, K.; Ito, T.; Asada, M.; Nakanishi, S.; Ding, P.; Lanford, W. A.; Hjorvarsson, B. *Surf. Sci.* **1997**, *387*, 320. Feibelman, P. J.; Hamman, D. R. *Surf. Sci.* **1987**, *182*, 411. Koeleman, B. J. J.; de Zwart, S. T.; Boers, A. L.; Poelsema, B.; Verhey, L. K. *Phys. Rev. Lett.* **1986**, *56*, 1152.